PERGAMON

Journal of Quantitative Spectroscopy & Radiative Transfer 79–80 (2003) 1139–1157

Journal of Quantitative Spectroscopy & Radiative Transfer

www.elsevier.com/locate/jqsrt

Enhanced lidar backscattering by quasi-horizontally oriented ice crystal plates in cirrus clouds

Ping Yang[a,*], Yong X. Hu[b], David M. Winker[b], Jun Zhao[c], Chris A. Hostetler[b], Lamont Poole[b], Bryan A. Baum[b], Michael I. Mishchenko[d], Jens Reichardt[e,f]

[a] *Department of Atmospheric Sciences, Texas A&M University, TAMU 3150, College Station, TX 77843, USA*
[b] *NASA Langley Research Center, MS 420, Hampton, VA 23681, USA*
[c] *Department of Mathematics, Texas A&M University, College Station, TX 77843, USA*
[d] *NASA Goddard Institute for Space Studies, New York, NY 10025, USA*
[e] *JCET, University of Maryland Baltimore County, Baltimore, MD 21250, USA*
[f] *Code 916, NASA Goddard Space Flight Center, Greenbelt, MD 20771, USA*

Received 20 May 2002; accepted 1 September 2002

Abstract

The backscattering of light by quasi-horizontally oriented hexagonal ice plates is investigated because of its pertinence to lidar measurements of cirrus clouds. For oriented ice crystals, the commonly used geometric optics ray-tracing method is not applicable to the computation of the scattered field in certain scattering directions, in particular, the backscattering direction, because of the singularity problem inherent to the ray-tracing technique. In this study, we solve for the electric field due to scattering by quasi-horizontally oriented ice plates using an approach based on the electromagnetic wave theory. We simplify the analysis by ignoring the effect of the plate's side faces on the internal field inside the particle. This is a reasonable approximation when the ratio of the particle diameter to its thickness is large. This approximation is also valid if the tilt of the particle's symmetric axis from zenith is small and the size parameter is large. The present numerical results indicate that very strong oscillations in the backscattering cross section occur with the variation of size parameter. Furthermore, the bulk backscattering intensity has been calculated by including the effect of a particle size distribution and the random tilt of particle symmetric axis within a small angular region, for example, 2°. A strong dependence is found between the lidar backscattering cross section and the degree of the random tilt of the particles. A combination of the present method with the T-matrix method, which works well for particles having small and moderate size parameters, may provide a more complete picture of the lidar backscattering by quasi-horizontally oriented ice plates.
© 2003 Elsevier Science Ltd. All rights reserved.

Keywords: Lidar; Backscattering; Ice plates; Cirrus clouds

* Corresponding author. Tel.: +1-979-845-4923; fax: +1-979-862-4466.
E-mail address: pyang@ariel.met.tamu.edu (P. Yang).

0022-4073/03/$ - see front matter © 2003 Elsevier Science Ltd. All rights reserved.
doi:10.1016/S0022-4073(02)00346-1

1. Introduction

Analyses based on the data from the Shuttle-based Lidar In-space Technology Experiment (LITE) showed the utility of spaceborne lidar returns for the retrieval of the microphysical properties of cirrus clouds [1]. The upcoming Cloud-Aerosol Lidar and Infrared Pathfinder Satellite Observations (CALIPSO, previously named PICASSO-CENA) mission, featuring a two-wavelength polarization sensitive lidar, an imaging infrared radiometer, and a wide field camera, will provide an unprecedented data set for the study of global cirrus cloud properties [2].

To interpret the data from spaceborne lidar, it is critically important to have a basic understanding of the backscattering by ice crystals with various shapes (habits) and orientations in space. These backscattering properties are useful to the identification of cloud phase [3]. A thorough understanding of the backscattering properties helps improve various aspects of CALIPSO lidar algorithms, such as calibration of 1064-nm channel and estimation of the extinction to backscattering ratio to be used in backscatter and extinction retrievals, as well as the treatment of multiple scattering. Previous ground-based lidar studies [4,5] have shown that cirrus clouds can produce enhanced backscattering. Theoretical studies have investigated the issue of backscattering enhancement by using the T-matrix method [6] and ray optics (e.g., [7]) to calculate the optical properties of plate ice particles. The ray-tracing technique can explain certain aspects of lidar backscattering characteristics of ice crystals [7]. However, it is not always appropriate to apply the ray optics method to the backscattering calculations because of the inherent singularity involved in ray optics, known as delta transmission/reflection, noted by Takano and Liou [8] and by Mishchenko and Macke [9]. To circumvent the shortcomings of the ray optics approach, a recent study by Iwasaki and Okamoto [10] treats backscattering as an external reflection that is mapped to the far field on the basis of Kirchhoff's diffraction approximation (KDA). It has been suggested by Stratton and Chu [11] that KDA is not mathematically well posed as either a Dirichlet problem or a Neumann problem. In addition, in Iwasaki and Okamoto's [10] analysis, the effect of the multiple internal reflections is ignored. As a result, the applicability of the KDA method may be limited because of the inaccuracy inherent to KDA.

The present study of lidar backscattering by quasi-horizontally oriented ice plates is based on the understanding that the effect of side faces is insignificant if the tilt angle of the particle c-axis from the zenith is small and the size parameter is large (>50). In this case, the internal field inside an ice crystal can be calculated analytically by applying the electromagnetic boundary conditions at two basal faces of the particle; subsequently, the internal field can be mapped to the far field in any scattering direction without introducing extra errors. Based on this analysis, the backscattering and depolarization properties of horizontally oriented ice plates are studied, especially for the ice crystals with large size parameters. This study, combined with a T-matrix solution [6,12] that works well for particles of small and moderate size parameters, will provide a much more complete picture of the backscattering properties of ice crystals. This paper is organized as follows. In Section 2, we present the theoretical basis for the light scattering computation associated with nearly horizontally oriented plates. In Section 3, we present numerical computation and discussions. Finally, the conclusions of this paper will be given in Section 4.

2. Theoretical basis

2.1. Coordinate systems

In this study, we consider the scattering of an electromagnetic wave by a hexagonal plate for which the symmetric axis is nearly vertically oriented. To calculate the scattering properties of the scattering particle, proper coordinate systems must be defined for the particle morphology and for the incidence and scattering configurations. The two diagrams in the first row of Fig. 1 show a coordinate system $OX_pY_pZ_p$ that is confined to the scattering particle. This coordinate system rotates with the particle if the particle rotates, and is hereafter referred to as the particle system. Diagram (C) in Fig. 1 shows the relative orientation of the scattering coordinate system $OX_sY_sZ_s$ with respect to a spatially fixed coordinate system or the so-called laboratory reference frame $OXYZ$. The coordinate axis OZ_s denotes the scattering direction and is confined to the plane YOZ in the present study. Diagrams (D)–(F) in Fig. 1 illustrate the transformation from the laboratory reference frame to that of the particle system. $OX_rY_rZ_r$ and $OX'_pY'_pZ'_p$ are two intermediate coordinate systems defined for the transformation from $OXYZ$ to $OX_pY_pZ_p$. Note that we allow the symmetric axis of the particle to randomly rotate around OZ axis in this study and hence φ_p is a random variable. To account for the azimuthal dependence of scattered field, it is equivalent to either rotate the particle with respect to the spatially fixed laboratory system or to vary the azimuthal angle of the scattering plane. The angle α_p, defined as a random variable distributed between 0 and $\pi/3$, denotes the rotation of the particle around its symmetric axis. Transformations between two of the four coordinate systems shown in Fig. 1 can be given as follows:

$$(x_p, y_p, z_p)^T = \Gamma_1(x'_p, y'_p, z'_p)^T, \tag{1a}$$

$$(x'_p, y'_p, z'_p)^T = \Gamma_2(x_r, y_r, z_r)^T \tag{1b}$$

$$(x_r, y_r, z_r)^T = \Gamma_3(x, y, z)^T, \tag{1c}$$

$$(x, y, z)^T = \Gamma_4(x_s, y_s, z_s)^T, \tag{1d}$$

where the superscript T denotes matrix transpose. The four rotational matrices involved in Eqs. (1a)–(1d) are given by

$$\Gamma_1 = \begin{bmatrix} \cos\alpha_p & \sin\alpha_p & 0 \\ -\sin\alpha_p & \cos\alpha_p & 0 \\ 0 & 0 & 1 \end{bmatrix}, \tag{1e}$$

$$\Gamma_2 = \begin{bmatrix} 1 & 0 & 0 \\ 0 & \cos\theta_p & -\sin\theta_p \\ 0 & \sin\theta_p & \cos\theta_p \end{bmatrix}, \tag{1f}$$

$$\Gamma_3 = \begin{bmatrix} \cos\varphi_p & \sin\varphi_p & 0 \\ -\sin\varphi_p & \cos\varphi_p & 0 \\ 0 & 0 & 1 \end{bmatrix}, \tag{1g}$$

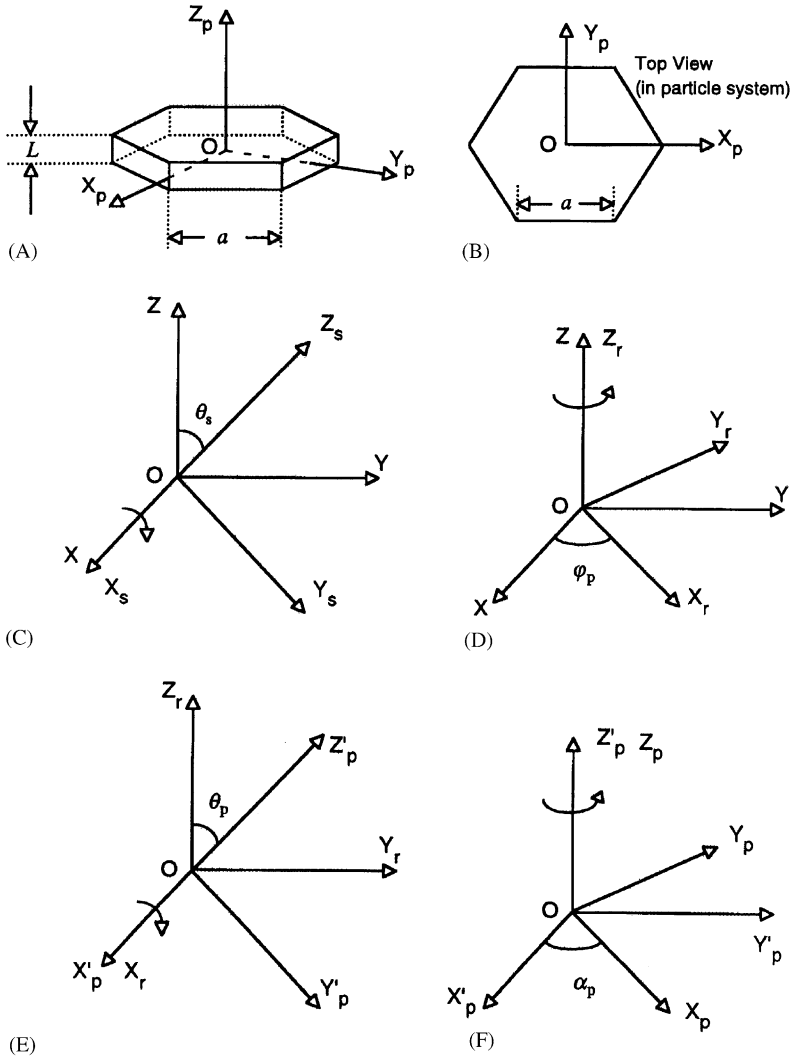

Fig. 1. Coordinate systems defined for particle, incidence geometry and scattering configuration. $OX_pY_pZ_p$ is particle geometry defined as being fixed with respect to the scattering particle. $OXYZ$ is a spatial coordinate system with z-axis along the propagating direction of the incident wave. $OX_sY_sZ_s$ is the scattering system, and $OX_rY_rZ_r$ and $OX'_pY'_pZ'_p$ the intermediate coordinate systems for the transformation between $OX_pY_pZ_p$ and $OX_sY_sZ_s$.

$$\Gamma_4 = \begin{bmatrix} 1 & 0 & 0 \\ 0 & \cos\theta_s & \sin\theta_s \\ 0 & -\sin\theta_s & \cos\theta_s \end{bmatrix}. \tag{1h}$$

Accordingly, the transformation between the scattering system and the particle system is given by

$$(x_p, y_p, z_p)^T = \Gamma(x_s, y_s, z_s)^T, \tag{2a}$$

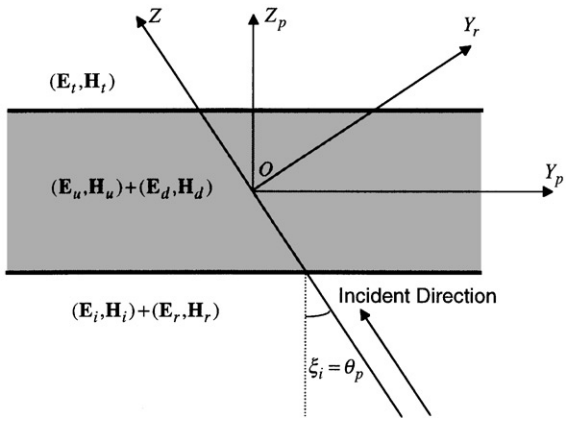

Fig. 2. Three spatial regions for incident and induced (scattered) electromagnetic fields associated with the scattering of an electromagnetic wave by a quasi-horizontally oriented hexagonal plate.

where

$$\Gamma = \begin{bmatrix} \Gamma_{11} & \Gamma_{12} & \Gamma_{13} \\ \Gamma_{21} & \Gamma_{22} & \Gamma_{23} \\ \Gamma_{31} & \Gamma_{32} & \Gamma_{33} \end{bmatrix} = \Gamma_1\Gamma_2\Gamma_3\Gamma_4. \tag{2b}$$

2.2. Upward and downward electromagnetic waves inside particle

The present computation focuses on the scattering of the incident lidar beam. The incident beam is assumed to be vertically upward radiation. Under the condition that the tilt of c-axis of a hexagonal plate (i.e., θ_p) from the local zenith is small, the effect of the side faces of the particle can be neglected in solving the internal field if the size of the particle is much larger than the incident wavelength or the aspect ratio (i.e., L/a) is small. This can be illustrated in the case when $\theta_p = 0$. The propagation of the incident wave can be regarded as the propagation of geometric rays if the size of the particle is much larger than the incident wavelength. If $\theta_p = 0$, there are no interactions between the side faces and the rays because of the specific particle orientation with respect to the incident direction. Thus, in the geometric optics regime the effect of the side faces is insignificant if θ_p is small. On the other hand, the incident wave cannot be regarded as being composed of a number of rays if the size parameter is small. In this case, the side faces can affect the internal field. However, the effect of side faces is much smaller than the effect of basal faces if the aspect ratio, L/a, of the particle is small. Because we deal with the scattering of ice crystals at lidar wavelengths for which the size parameters are normally large, we can ignore the effect of side faces for nearly horizontally orientated ice plates.

In the aforementioned situation, there are three distinct regions that are defined with respect to the particle system for the electromagnetic field, as shown in Fig. 2. For the region below the basal face of the particle, the field is composed of the incident field and reflected field. The reflected field contains a component that undergoes the multiple internal reflection inside the particles. For the

region above the upper basal face, the field is associated with transmitted wave that also includes the multiple internal reflection effect. Inside the particle, the total electromagnetic wave can be decomposed into an upward propagating wave and a downward traveling wave. Because the phase must be continuous for these waves at the boundaries (i.e., the upper and lower basal faces), the electric fields expressed with respect to the particle system can be written in a form similar to that in [13] as follows:

$$\mathbf{E}_{\mathrm{i}}(x_{\mathrm{p}}, y_{\mathrm{p}}, z_{\mathrm{p}}) = (E_{\mathrm{i}ox}\hat{x}_{\mathrm{p}} + E_{\mathrm{i}oy}\hat{y}_{\mathrm{p}} + E_{\mathrm{i}oz}\hat{z}_{\mathrm{p}})\exp\{\mathrm{i}k(-\sin\xi_{\mathrm{i}}y_{\mathrm{p}} + \cos\xi_{\mathrm{i}}z_{\mathrm{p}})\}, \tag{3a}$$

$$\mathbf{E}_{\mathrm{r}}(x_{\mathrm{p}}, y_{\mathrm{p}}, z_{\mathrm{p}}) = (E_{\mathrm{r}ox}\hat{x}_{\mathrm{p}} + E_{\mathrm{r}oy}\hat{y}_{\mathrm{p}} + E_{\mathrm{r}oz}\hat{z}_{\mathrm{p}})\exp\{\mathrm{i}k(-\sin\xi_{\mathrm{i}}y_{\mathrm{p}} - \cos\xi_{\mathrm{i}}z_{\mathrm{p}})\}, \tag{3b}$$

$$\mathbf{E}_{\mathrm{u}}(\mathbf{x}_{\mathrm{p}}, y_{\mathrm{p}}, z_{\mathrm{p}}) = E_{\mathrm{u}ox}\hat{x}_{\mathrm{p}} + E_{\mathrm{u}oy}\hat{y}_{\mathrm{p}} + E_{\mathrm{u}oz}\hat{z}_{\mathrm{p}})\exp\{-\mathrm{i}k[N_{\mathrm{r}}\sin\xi_t y_{\mathrm{p}} - (N_{\mathrm{r}}\cos\xi_t + \mathrm{i}N_n)z_{\mathrm{p}}]\}, \tag{3c}$$

$$\mathbf{E}_{\mathrm{d}}(x_{\mathrm{p}}, y_{\mathrm{p}}, z_{\mathrm{p}}) = (E_{\mathrm{d}ox}\hat{x}_{\mathrm{p}} + E_{\mathrm{d}oy}\hat{y}_{\mathrm{p}} + E_{\mathrm{d}oz}\hat{z}_{\mathrm{p}})\exp\{-\mathrm{i}k[N_{\mathrm{r}}\sin\xi_t y_{\mathrm{p}} + (N_{\mathrm{r}}\cos\xi_t + \mathrm{i}N_n)z_{\mathrm{p}}]\}, \tag{3d}$$

$$\mathbf{E}_t(x_{\mathrm{p}}, y_{\mathrm{p}}, z_{\mathrm{p}}) = (E_{tox}\hat{x}_{\mathrm{p}} + E_{toy}\hat{y}_{\mathrm{p}} + E_{toz}\hat{z}_{\mathrm{p}})\exp\{\mathrm{i}k(-\sin\xi_{\mathrm{i}}y_{\mathrm{p}} + \cos\xi_{\mathrm{i}}z_{\mathrm{p}})\}, \tag{3e}$$

where $\hat{x}_{\mathrm{p}}$, $\hat{y}_{\mathrm{p}}$, and $\hat{z}_{\mathrm{p}}$ are unit vectors along the three coordinate axes of the particle system. $k = 2\pi/\lambda$ is the wave number of the incident wave, with λ being the incident wavelength in vacuum. Note that the time dependence is assumed to be $\exp(-\mathrm{i}\omega t)$ for a harmonic electromagnetic wave in this study. N_{r} and N_n are effective refractive index. According to the study by Yang and Liou [14], these two parameters are given by

$$N_{\mathrm{r}} = 2^{-1/2}\{m_{\mathrm{r}}^2 - m_{\mathrm{i}}^2 + \sin^2\zeta_{\mathrm{i}} + [(m_{\mathrm{r}}^2 - m_{\mathrm{i}}^2 - \sin^2\zeta_{\mathrm{i}})^2 + 4m_{\mathrm{r}}^2 m_{\mathrm{i}}^2]^{1/2}\}^{1/2}, \tag{4a}$$

$$N_n = 2^{-1/2}\{-(m_{\mathrm{r}}^2 - m_{\mathrm{i}}^2 - \sin^2\zeta_{\mathrm{i}}) + [(m_{\mathrm{r}}^2 - m_{\mathrm{i}}^2 - \sin^2\zeta_{\mathrm{i}})^2 + 4m_{\mathrm{r}}^2 m_{\mathrm{i}}^2]^{1/2}\}^{1/2}, \tag{4b}$$

where m_{r} and m_{i} are the real and imaginary parts of the refractive index, respectively. The parameter, ξ_{i}, is the incident angle for the initial wave at the basal face, which is equal to the tilt of the particle for the incident geometry considered in this study:

$$\xi_{\mathrm{i}} = \theta_{\mathrm{p}}. \tag{5a}$$

The angle, ξ_t, is the angle of refraction at the basal face and is given by

$$\sin\xi_t = \sin\xi_{\mathrm{i}}/N_{\mathrm{r}}. \tag{5b}$$

The electric and magnetic fields are associated with each other via Maxwell's equations as follows:

$$\mathbf{H} = \frac{1}{\mathrm{i}k}\nabla \times \mathbf{E}, \tag{6a}$$

$$\mathbf{E} = -\frac{1}{\mathrm{i}k\varepsilon}\nabla \times \mathbf{H}, \tag{6b}$$

where the parameter ε is permittivity, given by

$$\varepsilon = (m_{\mathrm{r}}^2 - m_{\mathrm{i}}^2) + \mathrm{i}2m_{\mathrm{r}}m_{\mathrm{i}}. \tag{6c}$$

The electric fields in Eqs. (3b)–(3e) can be determined in terms of the incident field specified by Eq. (3a) based on the boundary conditions at two basal faces.

At the lower boundary (i.e., the lower basal face of the hexagonal plate):

$$\hat{z}_{\mathrm{p}} \times (\mathbf{E}_{\mathrm{i}} + \mathbf{E}_{\mathrm{r}} - \mathbf{E}_{\mathrm{u}} - \mathbf{E}_{\mathrm{d}}) = 0 \quad \text{and} \quad \hat{z}_{\mathrm{p}} \times (\mathbf{H}_{\mathrm{i}} + \mathbf{H}_{\mathrm{r}} - \mathbf{H}_{\mathrm{u}} - \mathbf{H}_{\mathrm{d}}) = 0. \tag{7a}$$

At the upper boundary (i.e., the upper basal face of the hexagonal plate):

$$\hat{z}_{\mathrm{p}} \times (\mathbf{E}_{t} - \mathbf{E}_{\mathrm{u}} - \mathbf{E}_{\mathrm{d}}) = 0 \quad \text{and} \quad \hat{z}_{\mathrm{p}} \times (\mathbf{H}_{t} - \mathbf{H}_{\mathrm{u}} - \mathbf{H}_{\mathrm{d}}) = 0. \tag{7b}$$

The incident field can be expressed in terms of two components, $E_{\mathrm{i,p,\parallel}}$ and $E_{\mathrm{i,p,\perp}}$, which are parallel and perpendicular to the incident plane OZZ_{p} (see Fig. 2), respectively. Using Eqs. (3a)–(3e), (6a), (6b), (7a) and (7b), the electric field inside the particle can be given as

$$\begin{bmatrix} E_{\mathrm{u}ox} \\ E_{\mathrm{u}oy} \\ E_{\mathrm{u}oz} \end{bmatrix} = \begin{bmatrix} 0 & T_{\mathrm{u}ox} \\ T_{\mathrm{u}oy} & 0 \\ T_{\mathrm{u}oz} & 0 \end{bmatrix} \begin{bmatrix} E_{\mathrm{i,p,\parallel}} \\ E_{\mathrm{i,p,\perp}} \end{bmatrix}, \tag{8a}$$

$$\begin{bmatrix} E_{\mathrm{d}ox} \\ E_{\mathrm{d}oy} \\ E_{\mathrm{d}oz} \end{bmatrix} = \begin{bmatrix} 0 & T_{\mathrm{d}ox} \\ T_{\mathrm{d}oy} & 0 \\ T_{\mathrm{d}oz} & 0 \end{bmatrix} \begin{bmatrix} E_{\mathrm{i,p,\parallel}} \\ E_{\mathrm{i,p,\perp}} \end{bmatrix}. \tag{8b}$$

The elements of the two transformation matrices in the preceding equations are given by

$$T_{\mathrm{u}ox} = \frac{2\cos\xi_{\mathrm{i}}(N_{\mathrm{r}}\cos\xi_t + \mathrm{i}N_n + \cos\xi_{\mathrm{i}})\exp[-\mathrm{i}k(N_{\mathrm{r}}\cos\xi_t + \mathrm{i}N_n + \cos\xi_{\mathrm{i}})L/2]}{T_a}, \tag{9a}$$

$$T_{\mathrm{d}ox} = \frac{2\cos\xi_{\mathrm{i}}(N_{\mathrm{r}}\cos\xi_t + \mathrm{i}N_n - \cos\xi_{\mathrm{i}})\exp[\mathrm{i}k(N_{\mathrm{r}}\cos\xi_t + \mathrm{i}N_n - \cos\xi_{\mathrm{i}})L/2]}{T_a}, \tag{9b}$$

$$T_{\mathrm{u}oy} = \frac{2\cos\xi_{\mathrm{i}}(N_{\mathrm{r}}\cos\xi_t + \mathrm{i}N_n)(\varepsilon\cos\xi_{\mathrm{i}} + N_{\mathrm{r}}\cos\xi_t + \mathrm{i}N_n)\exp[-\mathrm{i}k(\cos\xi_{\mathrm{i}} + N_{\mathrm{r}}\cos\xi_t + \mathrm{i}N_n)L/2]}{T_{\mathrm{b}}}, \tag{9c}$$

$$T_{\mathrm{d}oy} = \frac{2\cos\xi_{\mathrm{i}}(N_{\mathrm{r}}\cos\xi_t + \mathrm{i}N_n)(\varepsilon\cos\xi_{\mathrm{i}} - N_{\mathrm{r}}\cos\xi_t - \mathrm{i}N_n)\exp[-\mathrm{i}k(\cos\xi_{\mathrm{i}} - N_{\mathrm{r}}\cos\xi_t - \mathrm{i}N_n)L/2]}{T_{\mathrm{b}}}, \tag{9d}$$

$$T_{\mathrm{u}oz} = \frac{2\cos\xi_{\mathrm{i}}\sin\xi_{\mathrm{i}}(\varepsilon\cos\xi_{\mathrm{i}} + N_{\mathrm{r}}\cos\xi_t + \mathrm{i}N_n)\exp[-\mathrm{i}k(\cos\xi_{\mathrm{i}} + N_{\mathrm{r}}\cos\xi_t + \mathrm{i}N_n)L/2]}{T_{\mathrm{b}}} \tag{9e}$$

$$T_{\mathrm{d}oz} = -\frac{2\cos\xi_{\mathrm{i}}\sin\xi_{\mathrm{i}}(\varepsilon\cos\xi_{\mathrm{i}} - N_{\mathrm{r}}\cos\xi_t - \mathrm{i}N_n)\exp[-\mathrm{i}k(\cos\xi_{\mathrm{i}} - N_{\mathrm{r}}\cos\xi_t - \mathrm{i}N_n)L/2]}{T_{\mathrm{b}}}, \tag{9f}$$

where

$$\begin{aligned} T_a = {} & (\cos\xi_{\mathrm{i}} + N_{\mathrm{r}}\cos\xi_t + \mathrm{i}N_n)^2\exp[-\mathrm{i}k(N_{\mathrm{r}}\cos\xi_t + \mathrm{i}N_n)L] \\ & -(\cos\xi_{\mathrm{i}} - N_{\mathrm{r}}\cos\xi_t - \mathrm{i}N_n)^2\exp[\mathrm{i}k(N_{\mathrm{r}}\cos\xi_t + \mathrm{i}N_n)L], \end{aligned} \tag{9g}$$

$$T_{\mathrm{b}} = (\varepsilon\cos\xi_{\mathrm{i}} + N_{\mathrm{r}}\cos\xi_t + \mathrm{i}N_n)^2\exp[-\mathrm{i}k(N_{\mathrm{r}}\cos\xi_t + \mathrm{i}N_n)L]$$
$$-(\varepsilon\cos\xi_{\mathrm{i}} - N_{\mathrm{r}}\cos\xi_t - \mathrm{i}N_n)^2\exp[\mathrm{i}k(N_{\mathrm{r}}\cos\xi_t + \mathrm{i}N_n)L]. \tag{9h}$$

When the particle is absorptive (i.e., $m_{\mathrm{i}} \neq 0$), the electromagnetic wave inside the particle can be inhomogeneous, that is, the planes of wave phase contours are not parallel to the planes of wave amplitude contours. In this case, the electromagnetic wave may not be transverse with respect to the propagating direction of refracted wave, even in the geometric optics regime. It should be pointed out that the inhomogeneity of the wave has been fully accounted for in Eqs. (8) and (9).

2.3. Scattered field in far-field region

The scattered field in the radiation zone or the far-field region can be calculated in terms of the near-field scattering inside the particle (c.f., [15,16]) as follows:

$$\vec{E}^{\mathrm{s}}(\vec{r})|_{kr\to\infty} = \frac{k^2\mathrm{e}^{\mathrm{i}kr}}{4\pi r}(\varepsilon-1)\iiint_v\{\vec{E}(\vec{r}\,') - \hat{r}[\hat{r}\cdot\vec{E}(\vec{r}\,')]\}\mathrm{e}^{-\mathrm{i}k\hat{r}\cdot\vec{r}\,'}\,\mathrm{d}^3r', \tag{10}$$

where the integral domain, v, is the volume occupied by the scattering particle, and $\hat{r} = \mathbf{r}/|\mathbf{r}|$ is the scattering direction. Note that the scattering direction $\hat{r}$ is selected as $\hat{z}_{\mathrm{s}}$ in the present study, which can be expressed with respect to the particle system as follows:

$$\hat{r} = \Gamma_{13}\hat{x}_{\mathrm{p}} + \Gamma_{23}\hat{y}_{\mathrm{p}} + \Gamma_{33}\hat{z}_{\mathrm{p}}. \tag{11}$$

The scattered field in the radiation zone (i.e., the far-field region) is a transverse wave with respect to its propagating direction. Thus, we can decompose the corresponding electric field into two components that are parallel and perpendicular to the scattering plane (i.e., the OZZ_{s} plane in diagram D of Fig. 1) as follows:

$$\mathbf{E}^{\mathrm{s}} = E^{\mathrm{s}}_{\parallel}\hat{y}_{\mathrm{s}} + E^{\mathrm{s}}_{\perp}\hat{x}_{\mathrm{s}}. \tag{12}$$

According to Eqs. (3c), (3d), (8a), (8b), (10)–(12), the scattered far-field can be written in the form

$$\begin{bmatrix} E^{\mathrm{s}}_{\parallel} \\ E^{\mathrm{s}}_{\perp} \end{bmatrix} = \frac{k^2\exp(\mathrm{i}kr)(\varepsilon-1)}{4\pi r}\iiint_v \begin{bmatrix} \hat{y}_{\mathrm{s}}\cdot\hat{x}_{\mathrm{p}} & \hat{y}_{\mathrm{s}}\cdot\hat{y}_{\mathrm{p}} & \hat{y}_{\mathrm{s}}\cdot\hat{z}_{\mathrm{p}} \\ \hat{x}_{\mathrm{s}}\cdot\hat{x}_{\mathrm{p}} & \hat{x}_{\mathrm{s}}\cdot\hat{y}_{\mathrm{p}} & \hat{x}_{\mathrm{s}}\cdot\hat{z}_{\mathrm{p}} \end{bmatrix} \left\{ \begin{bmatrix} 0 & T_{\mathrm{u}ox} \\ T_{\mathrm{u}oy} & 0 \\ T_{\mathrm{u}oz} & 0 \end{bmatrix} \right.$$
$$\times\exp[\mathrm{i}k(N_{\mathrm{r}}\cos\xi_t + \mathrm{i}N_n)z_{\mathrm{p}}]$$
$$\left. + \begin{bmatrix} 0 & T_{\mathrm{d}ox} \\ T_{\mathrm{d}oy} & 0 \\ T_{\mathrm{d}oz} & 0 \end{bmatrix}\exp[-\mathrm{i}k(N_{\mathrm{r}}\cos\xi_t + \mathrm{i}N_n)z_{\mathrm{p}}] \right\} \begin{bmatrix} E_{\mathrm{i,p},\parallel} \\ E_{\mathrm{i,p},\perp} \end{bmatrix}$$
$$\times\exp(-\mathrm{i}k\sin\theta_{\mathrm{p}}y_{\mathrm{p}})\exp[-\mathrm{i}k(\Gamma_{13}x_{\mathrm{p}} + \Gamma_{23}y_{\mathrm{p}} + \Gamma_{33}z_{\mathrm{p}})]\,\mathrm{d}x_{\mathrm{p}}\,\mathrm{d}y_{\mathrm{p}}\,\mathrm{d}z_{\mathrm{p}}. \tag{13}$$

The decomposed components of the incident field in $OXYZ$ and $OX_rY_rZ_r$ systems are related via the following expression:

$$\mathbf{E}^{\mathrm{i}} = E^{\mathrm{i}}_{\parallel}\hat{y} + E^{\mathrm{i}}_{\perp}\hat{x} = E_{\mathrm{i,p},\parallel}\hat{y}_{\mathrm{r}} + E_{\mathrm{i,p},\perp}\hat{x}_{\mathrm{r}}, \tag{14}$$

or, in a matrix form as follows

$$\begin{bmatrix} E_{\mathrm{i,p},\parallel} \\ E_{\mathrm{i,p},\perp} \end{bmatrix} = \begin{bmatrix} \hat{y}_{\mathrm{r}}\cdot\hat{y} & \hat{y}_{\mathrm{r}}\cdot\hat{x} \\ \hat{x}_{\mathrm{r}}\cdot\hat{y} & \hat{x}_{\mathrm{r}}\cdot\hat{x} \end{bmatrix} \begin{bmatrix} E^{\mathrm{i}}_{\parallel} \\ E^{\mathrm{i}}_{\perp} \end{bmatrix} = \begin{bmatrix} \cos\varphi_{\mathrm{p}} & -\sin\varphi_{\mathrm{p}} \\ \sin\varphi_{\mathrm{p}} & \cos\varphi_{\mathrm{p}} \end{bmatrix} \begin{bmatrix} E^{\mathrm{i}}_{\parallel} \\ E^{\mathrm{i}}_{\perp} \end{bmatrix}. \tag{15}$$

Thus, the scattered field can be expressed in terms of incident field through the transformation of the scattering matrix as follows:

$$\begin{bmatrix} E^{\mathrm{S}}_{\parallel} \\ E^{\mathrm{S}}_{\perp} \end{bmatrix} = \frac{\exp(\mathrm{i}kr)}{-\mathrm{i}kr} \begin{bmatrix} S_2 & S_3 \\ S_4 & S_1 \end{bmatrix} \begin{bmatrix} E^{\mathrm{i}}_{\parallel} \\ E^{\mathrm{i}}_{\perp} \end{bmatrix}, \tag{16a}$$

where the scattering matrix is given by

$$\begin{aligned} \begin{bmatrix} S_2 & S_3 \\ S_4 & S_1 \end{bmatrix} = \frac{-\mathrm{i}k^3(\varepsilon-1)}{4\pi} \iiint_v \begin{bmatrix} \Gamma_{12} & \Gamma_{22} & \Gamma_{32} \\ \Gamma_{11} & \Gamma_{21} & \Gamma_{31} \end{bmatrix} \\ \times \left\{ \begin{bmatrix} 0 & T_{\mathrm{u}ox} \\ T_{\mathrm{u}oy} & 0 \\ T_{\mathrm{u}oz} & 0 \end{bmatrix} \exp[\mathrm{i}k(N_{\mathrm{r}}\cos\xi_t + \mathrm{i}N_n)z_{\mathrm{p}}] \right. \\ \left. + \begin{bmatrix} 0 & T_{\mathrm{d}ox} \\ T_{\mathrm{d}oy} & 0 \\ T_{\mathrm{d}oz} & 0 \end{bmatrix} \exp[-\mathrm{i}k(N_{\mathrm{r}}\cos\xi_t + \mathrm{i}N_n)z_{\mathrm{p}}] \right\} \begin{bmatrix} \cos\varphi_{\mathrm{p}} & -\sin\varphi_{\mathrm{p}} \\ \sin\varphi_{\mathrm{p}} & \cos\varphi_{\mathrm{p}} \end{bmatrix} \\ \times \exp(-\mathrm{i}k\sin\theta_{\mathrm{p}}y_{\mathrm{p}})\exp[-\mathrm{i}k(\Gamma_{13}x_{\mathrm{p}} + \Gamma_{23}y_{\mathrm{p}} + \Gamma_{33}z_{\mathrm{p}})]\,\mathrm{d}x_{\mathrm{p}}\,\mathrm{d}y_{\mathrm{p}}\,\mathrm{d}z_{\mathrm{p}}. \end{aligned} \tag{16b}$$

The volume integration involved in Eq. (16b) can be analytically solved for a hexagonal plate. Accordingly, an explicit form of the scattering matrix can be obtained as follows:

$$\begin{aligned} &\begin{bmatrix} S_2 & S_3 \\ S_4 & S_1 \end{bmatrix} \\ &= \frac{-\sqrt{3}k^3(\varepsilon-1)a^2L}{8\pi} f \\ &\times \left\{ S_{\mathrm{u}} \frac{\exp(-kN_nL/2)\exp[\mathrm{i}k(N_{\mathrm{r}}\cos\xi_t - \Gamma_{33})L/2] - \exp(kN_nL/2)\exp[-\mathrm{i}k(N_{\mathrm{r}}\cos\xi_t - \Gamma_{33})L/2]}{k(N_{\mathrm{r}}\cos\xi_t - \Gamma_{33})L + \mathrm{i}kN_nL} \right. \\ &\left. + S_{\mathrm{d}} \frac{\exp(-kN_nL/2)\exp[\mathrm{i}k(N_{\mathrm{r}}\cos\xi_t + \Gamma_{33})L/2] - \exp(kN_nL/2)\exp[-\mathrm{i}k(N_{\mathrm{r}}\cos\xi_t + \Gamma_{33})L/2]}{k(N_{\mathrm{r}}\cos\xi_t + \Gamma_{33})L + \mathrm{i}kN_nL} \right\}, \end{aligned} \tag{17a}$$

where

$$f = \exp\{-\mathrm{i}[\Gamma_{13} + \sqrt{3}(\sin\theta_\mathrm{p} + \Gamma_{23})]ka/4\} \cdot \frac{\sin(\Gamma_{13}ka/2)}{\Gamma_{13}ka/2} \cdot \frac{\sin\{[\Gamma_{13} - \sqrt{3}(\sin\theta_\mathrm{p} + \Gamma_{23})]ka/4\}}{[\Gamma_{13} - \sqrt{3}(\sin\theta_\mathrm{p} + \Gamma_{23})]ka/4}$$
$$+ \exp(\mathrm{i}\Gamma_{13}ka/2)\frac{\sin\{[\Gamma_{13} - \sqrt{3}(\sin\theta_\mathrm{p} + \Gamma_{23})]ka/4\}}{[\Gamma_{13} - \sqrt{3}(\sin\theta_\mathrm{p} + \Gamma_{23})]ka/4} \cdot \frac{\sin\{[\Gamma_{13} + \sqrt{3}(\sin\theta_\mathrm{p} + \Gamma_{23})]ka/4\}}{[\Gamma_{13} + \sqrt{3}(\sin\theta_\mathrm{p} + \Gamma_{23})]ka/4}$$
$$+ \exp\{-\mathrm{i}[\Gamma_{13} - \sqrt{3}(\sin\theta_\mathrm{p} + \Gamma_{23})]ka/4\} \cdot \frac{\sin(\Gamma_{13}ka/2)}{\Gamma_{13}ka/2}$$
$$\times \frac{\sin\{[\Gamma_{13} + \sqrt{3}(\sin\theta_\mathrm{p} + \Gamma_{23})]ka/4\}}{[\Gamma_{13} + \sqrt{3}(\sin\theta_\mathrm{p} + \Gamma_{23})]ka/4}, \tag{17b}$$

$$S_\mathrm{u} = \begin{bmatrix} \Gamma_{12} & \Gamma_{22} & \Gamma_{32} \\ \Gamma_{11} & \Gamma_{21} & \Gamma_{31} \end{bmatrix} \begin{bmatrix} 0 & T_{\mathrm{u}ox} \\ T_{\mathrm{u}oy} & 0 \\ T_{\mathrm{u}oz} & 0 \end{bmatrix} \begin{bmatrix} \cos\varphi_\mathrm{p} & -\sin\varphi_\mathrm{p} \\ \sin\varphi_\mathrm{p} & \cos\varphi_\mathrm{p} \end{bmatrix}, \tag{17c}$$

$$S_\mathrm{d} = \begin{bmatrix} \Gamma_{12} & \Gamma_{22} & \Gamma_{32} \\ \Gamma_{11} & \Gamma_{21} & \Gamma_{31} \end{bmatrix} \begin{bmatrix} 0 & T_{\mathrm{d}ox} \\ T_{\mathrm{d}oy} & 0 \\ T_{\mathrm{d}oz} & 0 \end{bmatrix} \begin{bmatrix} \cos\varphi_\mathrm{p} & -\sin\varphi_\mathrm{p} \\ \sin\varphi_\mathrm{p} & \cos\varphi_\mathrm{p} \end{bmatrix}. \tag{17d}$$

2.4. Single-scattering properties

After the scattering matrix is calculated, it is straightforward to calculate the single-scattering properties of the particle. The extinction and scattering cross sections depend on the configuration of incident polarization. However, if the extinction cross section is averaged for the incident polarization, it can be given by

$$\sigma_\mathrm{ext} = \frac{1}{2}(\sigma_{\mathrm{ext},\parallel} + \sigma_{\mathrm{ext},\perp}) = \frac{2\pi}{k^2} Re\{S_1(0) + S_2(0)\}. \tag{18}$$

In Eq. (18), $\sigma_{\mathrm{ext},\parallel}$ and $\sigma_{\mathrm{ext},\perp}$ denote the extinction cross sections for parallel and perpendicular polarization, respectively. Similarly, for the scattering cross section, we have

$$\sigma_\mathrm{sca} = \frac{1}{2}(\sigma_{\mathrm{sca},\parallel} + \sigma_{\mathrm{sca},\perp})$$
$$= \frac{1}{2k^2}\int_0^\pi \int_0^{2\pi} (|S_1|^2 + |S_2|^2 + |S_3|^2 + |S_4|^2)\sin\theta_\mathrm{p}\,\mathrm{d}\theta_\mathrm{p}\,\mathrm{d}\varphi_\mathrm{p}. \tag{19}$$

The projected area of the hexagonal particle is

$$A = 2aL\sin\theta_\mathrm{p} + \frac{3\sqrt{3}}{2}a^2\cos\theta_\mathrm{p}. \tag{20}$$

The extinction and scattering efficiencies are thus given by

$$Q_\mathrm{ext} = \sigma_\mathrm{ext}/A \quad \text{and} \quad Q_\mathrm{sca} = \sigma_\mathrm{sca}/A. \tag{21}$$

The transformation of the incident to the scattered Stokes vectors is given by

$$\begin{bmatrix} I_s \\ Q_s \\ U_s \\ V_s \end{bmatrix} = \frac{\sigma_{sca}}{4\pi r^2} P_{11} \begin{bmatrix} 1 & P_{12}/P_{11} & P_{13}/P_{11} & P_{14}/P_{11} \\ P_{21}/P_{11} & P_{22}/P_{11} & P_{23}/P_{11} & P_{24}/P_{11} \\ P_{31}/P_{11} & P_{32}/P_{11} & P_{33}/P_{11} & P_{34}/P_{11} \\ P_{41}/P_{11} & P_{42}/P_{11} & P_{43}/P_{11} & P_{44}/P_{11} \end{bmatrix} \begin{bmatrix} I_i \\ Q_i \\ U_i \\ V_i \end{bmatrix}, \tag{22}$$

where the definition of the phase matrix follows those of van de Hulst [17]. In Eq. (22) the first phase matrix element, P_{11}, is the normalized phase function given by

$$P_{11} = \frac{2\pi}{k^2 \sigma_{sca}} (|S_1|^2 + |S_2|^2 + |S_3|^2 + |S_4|^2). \tag{23}$$

After the normalized phase function is calculated, the lidar backscattering is given by

$$\sigma_b = \sigma_{sca} \cdot P_{11}(\theta_s = 180^\circ). \tag{24}$$

If the incident beam is unpolarized, that is $Q_i = U_i = V_i = 0$, we can define the degree of polarization (DP), the degree of linear polarization (DLP), and the degree of circular polarization (DCP) for the scattered wave as follows [18]:

$$DP = \frac{\sqrt{Q_s^2 + U_s^2 + V_s^2}}{I_s} = \left(\frac{P_{21}^2 + P_{31}^2 + P_{41}^2}{P_{11}^2} \right)^{1/2}, \tag{25}$$

$$DLP = -\frac{Q_s}{I_s} = -\frac{P_{21}}{P_{11}}, \tag{26}$$

$$DCP = \frac{V}{I} = \frac{P_{41}}{P_{11}}. \tag{27}$$

Most lasers generate linearly polarized radiation (i.e., $I_i = Q_i$ and $U_i = V_i = 0$). The linear depolarization ratio is

$$\delta_L = \frac{I_s - Q_s}{I_s + Q_s} = \frac{P_{11} + P_{12} - P_{21} - P_{22}}{P_{11} + P_{12} + P_{21} + P_{22}}. \tag{28}$$

In this study, we only consider the degree of linear polarization and the linear depolarization ratio in numerical computation.

3. Numerical results and discussions

For the ice plates involved in the present scattering calculation, the following relationship given by Pruppacher and Klett [19] is used:

$$L = 2.4883 a^{0.474}, \quad 5\ \mu\text{m} \leqslant a \leqslant 1500\ \mu\text{m}, \tag{29}$$

where L denotes plate thickness, and a denotes the semi-width of the particle cross section. Eq. (29) is the same as Eq. (4) in [20], but the units used in the present equation are microns.

Fig. 3 shows the phase function values for plates with a size of $D/L = 50\ \mu\text{m}/10\ \mu\text{m}$ where D is the diameter of the cross section and L the thickness of the plate. The wavelength is 0.532 μm, and the corresponding refractive index is $1.3117 + i2.6138 \times 10^{-9}$. The short horizontal bars in the

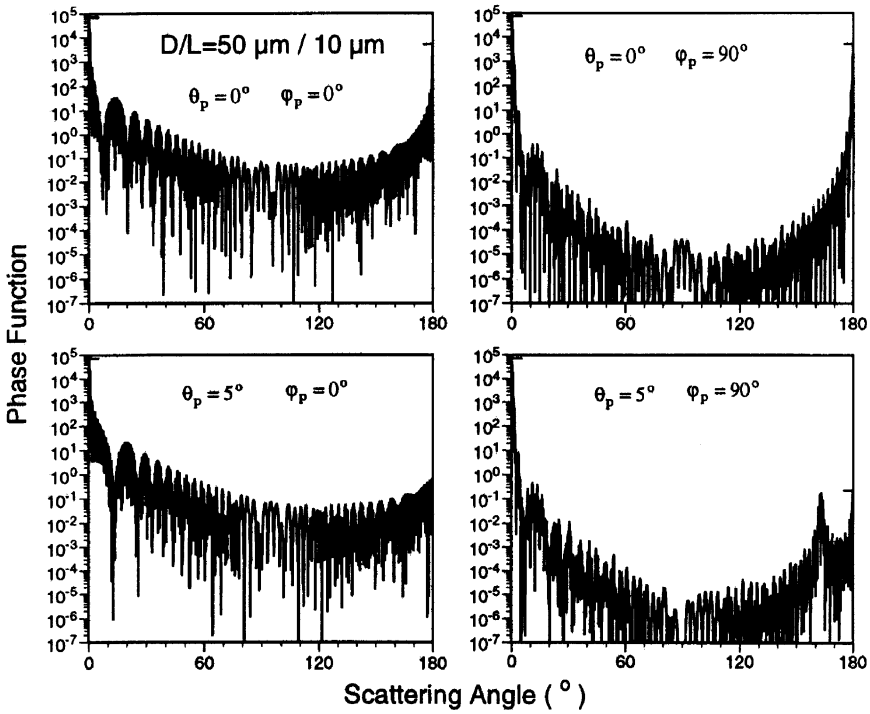

Fig. 3. The phase function of ice plates for two incident configurations ($\theta = 0°$ and $5°$) and view geometry with particle size of $D/L = 50$ μm/10 μm. The horizontal bars indicate the values of the phase function in forward and backscattering directions.

diagrams indicate the magnitudes of the phase functions in the forward and backscattering directions. The upper two panels are for the case when the symmetric axis of the particle is exactly vertically oriented. The lower two panels are for the case when the symmetric axis of the particle is tilted 5° from zenith. For specifically oriented particles, the scattered field depends not only on the scattering zenith angle but also on the azimuthal angle of the scattering plane. As evident from results shown in Fig. 3, the side scattering for the case with $\varphi_p = 90°$ is much smaller than for the case with $\varphi_p = 0°$. The scattering peak around 170° in the case of $\theta_p = 5°$ and 90° corresponds to the specular reflection of the incident light by the base face of the plate. One striking feature shown in Fig. 3 is the rapid oscillation of phase function versus the scattering angle, which is caused by the phase interference. This behavior is absent in the results derived from conventional ray-tracing techniques, in particular, by those numerical ray-tracing algorithms that ignore the phase interference. This phase interference pattern has been noted in the exact T-matrix results [6]. It should also be pointed out that the phase function derived from the ray-tracing technique for horizontally oriented plates is a superposition of the diffraction contribution and two Dirac delta functions, $\delta(\theta)$ and $\delta(\theta - \pi)$. This discontinuity is unrealistic and is inherent to the ray-tracing method.

Fig. 4 is the same as Fig. 3, except that the size of the plate is $D/L = 100$ μm/15 μm for Fig. 4. It is evident from the comparison of the two diagrams that an increase of particle size can substantially change the magnitude of the phase function in the side and backscattering directions. However, the

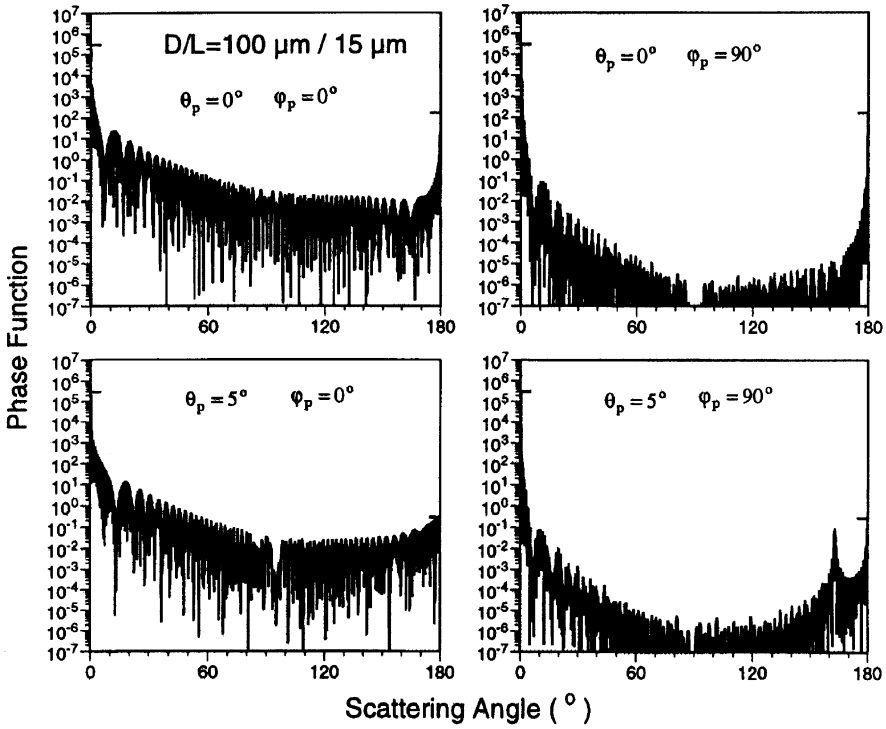

Fig. 4. Same as Fig. 3, except that the size is $D/L = 100$ μm/15 μm.

feature related to phase interface shows up when the symmetric axis of the particle is tilted away from zenith. At the 0.532 μm wavelength, absorption is negligible. Unlike the results calculated by the present method, the phase function derived from the conventional ray-tracing method is essentially independent of particle size in the side and backscattering directions. From Figs. 3 and 4, it can be seen that the backscatter at exactly 180° is sensitive to the tilt of the plates. A tilt of 5° can reduce the backscatter by a few orders in magnitude.

Fig. 5 shows the backscatter cross section, degree of linear polarization, and depolarization ratio for three tilt angles. 0°, 2°, and 5°. The oscillations associated with the resonant effect are evident from the variation of backscattering intensity versus particle size. In addition, the backscattering intensity is very sensitive to the tilt of the particle symmetric axis. As expected, the depolarization ratio of horizontally oriented plates is not significant.

To smooth out the resonant effect associated with the scattering by individual particles, we use a size distribution specified by a gamma function, given by

$$n(D) = N_0 D^{\gamma} \exp(-\gamma D/D_{\mathrm{m}}), \tag{30}$$

where N_0 is the total number of ice crystals in a unit volume; D is the maximum crystal dimension, and D_{m} is the modal size. Note that the analytical size distribution given by Eq. (30), if the parameters are specified properly, can be used to approximate in situ size distributions in some

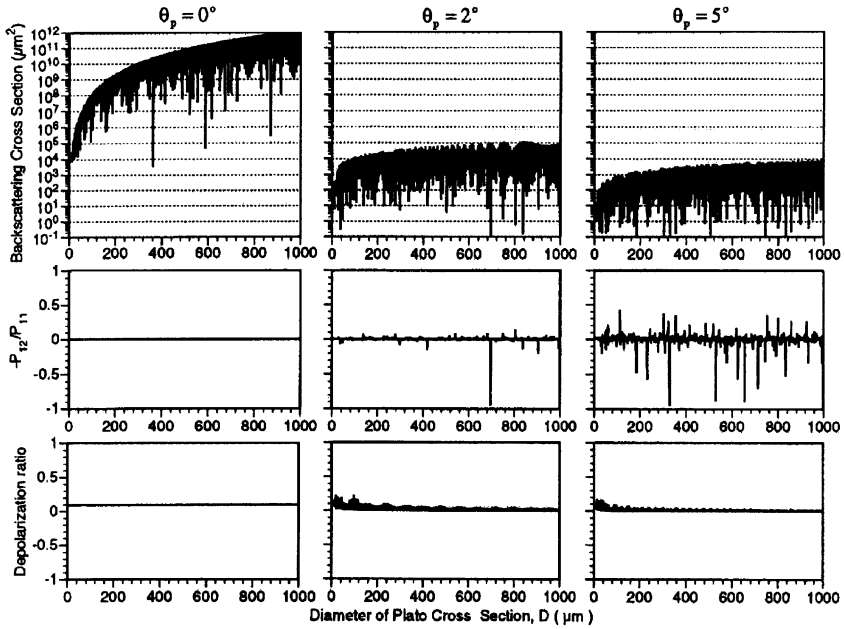

Fig. 5. The variations of backscattering cross sections, the degree of linear polarization, and depolarization versus particle size for three tilting angles: 0°, 2°, and 5°.

cases. For example, the size distribution observed on November 25, 1991 during the First ISCCP Regional Experiment (FIRE) phase II can be well represented by analytical expression given in Eq. (30), as is evident from Fig. 6.

It is common to define an effective size distribution as follows (e.g., [21]):

$$D_e = \frac{3}{2}\frac{\int_{D_1}^{D_2} V(D)n(D)\,\mathrm{d}D}{\int_{D_1}^{D_2} A(D)n(D)\,\mathrm{d}D}, \tag{31}$$

where V is the volume and A is the projected area of a ice crystal of the size of D. The bulk optical properties are mainly determined by the effective size, as is illustrated by Wyser and Yang [22]. The projected area of horizontally oriented plates can be larger relative to particle volume than randomly oriented plates. In addition, the effective size of horizontally oriented plates also depends on the random tilt of the particles. Fig. 7 shows the relationship between mean diameter and effective size for randomly tilted plates. The angle $\Delta\theta_p$ is the maximum magnitude of random tilt for the particles. Evidently, the difference between the effective sizes calculated for $\Delta\theta_p = 2°$ and 5° are essentially insignificant because of a small variation of the projected area. From Fig. 7, it can also be noted that the effective size can be small for a large mean diameter.

The CALIPSO lidar employs two wavelengths: 0.532 and 1.064 μm. The 0.532 μm channel is calibrated using molecular backscatter in the mid stratosphere (assumed free of aerosols); however, the 1.064 μm channel is difficult to calibrate by the same method due to a much lower signal-to-noise ratio for that region. Cloud backscatter signals can be used to transfer calibration from the 0.532 to

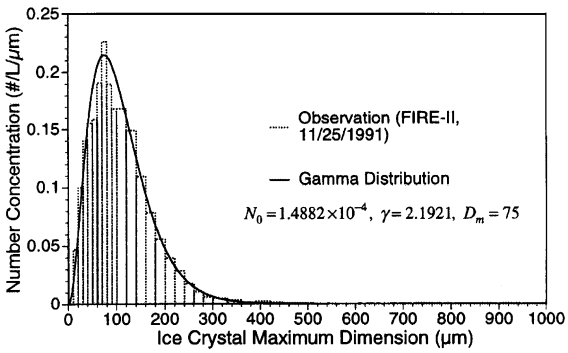

Fig. 6. The comparison between a gamma function with an in situ size distribution obtained during FIRE-II field campaign.

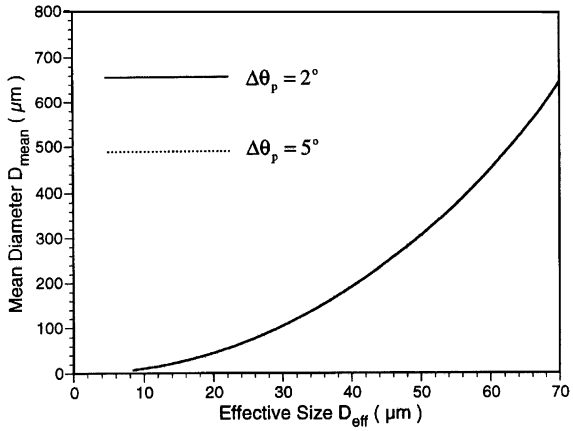

Fig. 7. The variation of mean diameter versus the effective diameter for maximum titling angles of $\Delta\theta_p = 2°$ and 5°.

the 1064 μm channel if the single-scattering properties at the two wavelengths are well characterized. Fig. 8 shows the comparison of the mean extinction efficiencies at 0.532 and 1.064 μm wavelengths and the relative difference as functions of the effective size. The refractive indices for these two wavelengths are $1.3117 + i2.6138 \times 10^{-9}$ and $1.3004 + i1.933 \times 10^{-6}$, respectively. For effective sizes larger than approximately 20 μm, the extinction efficiencies at these two wavelengths are essentially the same. For small effective sizes (less than approximately 10 μm), a difference on the order of 10% is noticed for the two extinction efficiencies.

Fig. 9 shows the backscattering cross section and backscattering efficiency (the ratio of backscattering cross section to projected area) at 0.532 and 1.064 μm wavelengths. For a given particle size, the size parameter for 1.064 μm is twice of that for 0.532 μm. Additionally, the absorption of radiation by ice crystals is slightly larger for 1.064 μm wavelength. The overall variation patterns for these two wavelengths are similar. However, the backscattering efficiency for the 1.064 μm wavelength is larger. The backscattering cross section increases with the increase of effective size because the average projected area of particles increases with the effective size. The backscattering efficiency, however, decreases with the increase of the effective size, which is mainly due to the destructive phase interference that is more significant for large size parameters as well as stronger forward scattering for larger plates.

In situ measurement of 180° backscattering is very challenging, if not impossible. Measurements at angles close to 180° (e.g., 179°) are made instead for estimating the lidar ratio. It is known that 180° backscattering for spherical ice particles at visible and near-IR wavelengths is much stronger than the backscattering at an angle slightly different from 180°. Our model predicts similar behavior for ice particles. Fig. 10 shows the ratio of phase function at 179.9° and 179.5° to the phase function value in the exact 180° backscattering direction. It can be seen that the scattered intensity is substantially reduced if the observation is made in a direction tilted slightly away from the exact backscattering direction. In addition, for effective sizes larger than approximately 30 μm, the ratio tends to reach its asymptotic value with respect to the variation of the effective size. In practice, lidar returns have a

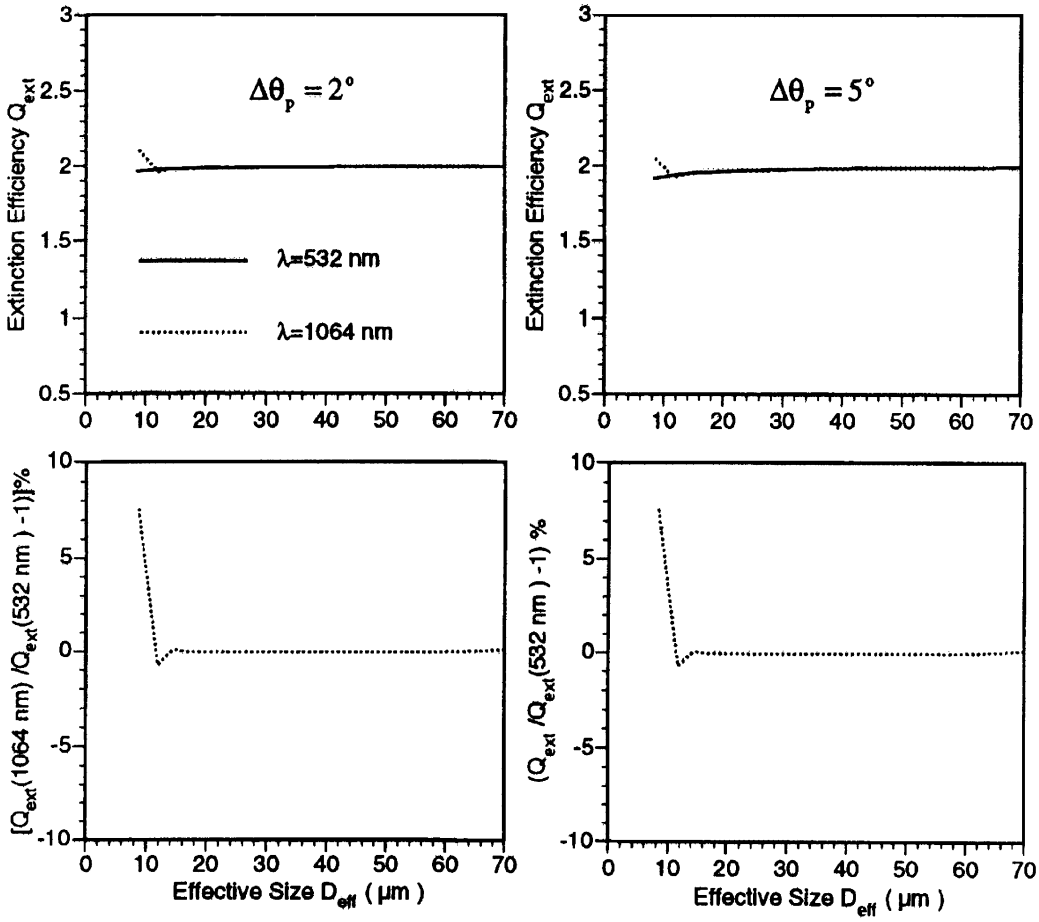

Fig. 8. The bulk extinction efficiency computed for 0.532 and 1.064 μm wavelengths. Also shown are the relative difference of the extinction efficiencies for the two wavelengths.

certain field of view, and it is critical to average the backscattering intensity over the field of view, as is discussed by Iwasaki and Okamoto [10].

4. Summary

We investigate the backscattering of light by quasi-horizontally oriented hexagonal ice plates because of its importance to lidar measurements of cirrus clouds. For the case of oriented ice crystals, a singularity problem in the geometric optics ray-tracing method limits its capability for the computation of the scattered field in certain scattering directions, particularly for the case of direct backscattering. To overcome the shortcomings of ray-tracing techniques for light scattering calculations involving horizontally oriented ice plates, we have developed a computational method

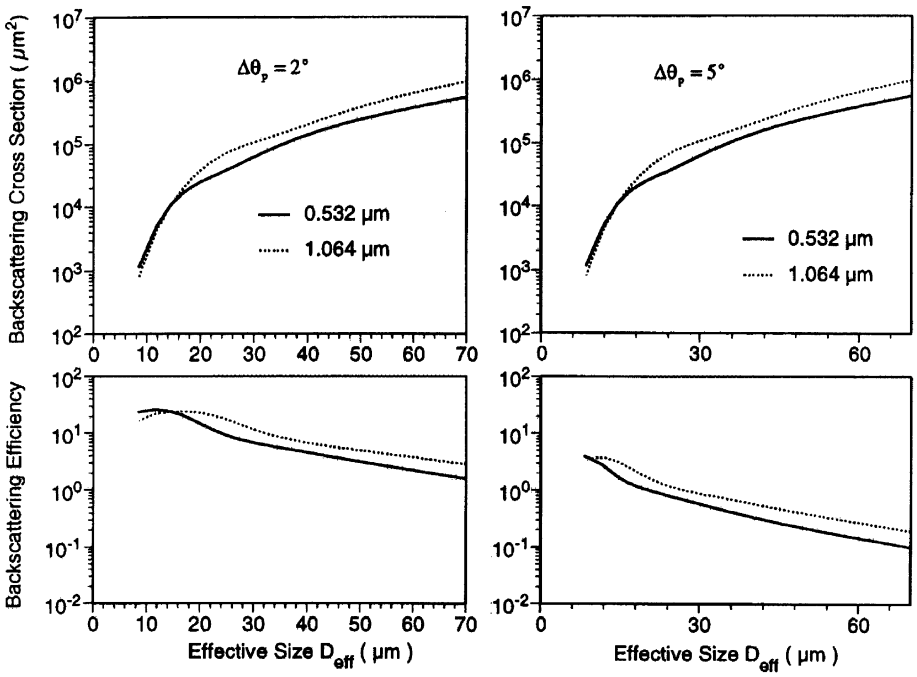

Fig. 9. The bulk backscattering cross section and efficiency as functions of effective size for 0.532 and 1.064 μm wavelengths.

that is based on electromagnetic wave theory. The approximation involved neglects the effect of the plate's side faces on the internal field calculation. Numerical computations have been carried out for the backscattering cross section and scattering polarization configuration for ice plates that are nearly horizontally oriented. The scattering computational algorithm developed in this study may be useful in computation of the enhanced lidar backscattering by ice plates.

While the extinction cross sections at the 532 and 1064 nm wavelengths are almost the same for plates larger in effective size than 20 μm, the backscattering cross sections at the two wavelengths are different. Single scattering at 1064 nm is stronger than at 532 nm. On the other hand, the delta transmission at 532 nm is larger than at 1064 nm. For ice clouds, lidar backscatter is due primarily to single scattering (direct backscattering) and double scattering (one forward scattering event plus one backscattering event). The backscattering cross section alone cannot reveal whether the backscattering at the two wavelengths are of the same magnitude for ice clouds of moderate to relatively high ice particle density. We will continue to investigate the relative magnitude of backscatter at the two wavelengths and the implication for cross calibration of the two CALIPSO lidar channels with an ongoing Monte Carlo multiple scattering simulation study.

In the atmosphere, the ice crystals in cirrus clouds have various particle habits. Ice columns (in particular, large columns) tend to orient with their *c*-axis in horizontal planes. We are currently investigating the scattering properties of horizontally oriented column ice crystals and their applications to active remote sensing based on lidar returns in a related ongoing study.

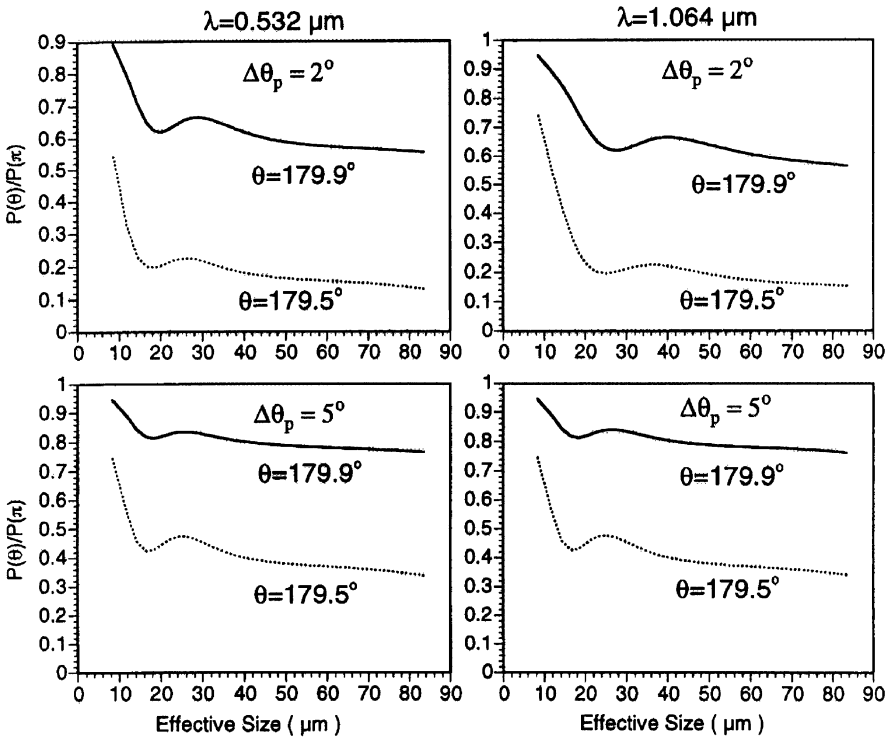

Fig. 10. The ratio of phase function values at scattering angles 179.9° and 179.5° to the phase function value at exact backscattering (180°).

Acknowledgements

This research has been supported by the NASA CALIPSO project, Cirrus Regional Study of Tropical Anvil and Cirrus Layers-Florida Area Cirrus Experiment (CRYSTAL-FACE), the NASA Radiation Science Program managed by Dr. Donald Anderson (NAG5-11374). J. Reichardt's research is supported by the NASA Atmospheric Chemistry Modeling and Analysis program managed by Dr. Phil DeCola.

References

[1] Winker DM, Couch RH, McCormick MP. An overview of LITE: NASA's lidar in-space technology experiment. Proc IEEE 1996;84:164–80.
[2] Winker DM, Wielicki BA. The PICASSO-CENA Mission. In: Fujisada H, editor. Sensors, systems, and next generation satellites. Proceedings of the SPIE, vol. 3870, 1999. 2636p.
[3] Hu YX, Winker DM, Yang P, Baum BA, Poole L, Vann L. Identification of cloud phase from PICASSO-CENA lidar depolarization: a multiple scattering sensitivity study. JQSRT 2001;70:569–79.
[4] Platt CM. Lidar backscatter from horizontal ice crystal plates. J Appl Meteorol 1978;17:482–8.
[5] Platt CM, Abshire NL, McNice GT. Some microphysical properties of an ice cloud from lidar observation of horizontally oriented crystals. J Appl Meteorol 1978;17:1220–4.

[6] Mishchenko MI, Wielaard DJ, Carlson BE. T-matrix computations of zenith-enhanced lidar backscattering from horizontally oriented ice plates. Geophys Res Lett 1997;24:771–4.
[7] Borovoi A, Grishin I, Naats E, Oppel U. Light backscattering by hexagonal ice crystals. JQSRT 2002;72:403–17.
[8] Takano Y, Liou KN. Solar radiative transfer in cirrus clouds. I. Single-scattering and optical properties of hexagonal ice crystals. J Atmos Sci 1989;46:3–19.
[9] Mishchenko MI, Macke A. Incorporation of physical optics effects and computation of Legendre expansion for ray-tracing phase functions involving delta-function transmission. J Geophys Res 1998;103:1799–805.
[10] Iwasaki S, Okamoto H. Analysis of the enhancement of backscattering by nonspherical particles with flat surfaces. Appl Opt 2001;40:6121–9.
[11] Stratton JA, Chu LJ. Diffraction theory of electromagnetic waves. Phys Rev 1939;56:99–107.
[12] Mishchenko MI. Calculation of the amplitude matrix for a nonspherical particle in a fixed orientation. Appl Opt 2000;39:1026–31.
[13] Yang P, Gao BC, Baum BA, Hu YX, Wiscombe WJ, Mishchenko MI, Winker DM, Nasiri SL. Asymptotic solutions for optical properties of large particles with strong absorption. Appl Opt 2001;40:1532–47.
[14] Yang P, Liou KN. Light scattering by hexagonal ice crystals: comparison of finite-difference time domain and geometric optics method. J Opt Soc Am A 1995;12:162–76.
[15] Goedeke GH, O'Brien SG. Scattering by irregular inhomogeneous particles via the digitized Green's function algorithm. Appl Opt 1988;27:2431–8.
[16] Yang P, Liou KN. Finite-difference time domain method for light scattering by small ice crystals in three-dimensional space. J Opt Soc Am A 1996;13:2072–85.
[17] van de Hulst HC. Light scattering by small particles. New York: Wiley, 1957.
[18] Bohren CF, Huffman DR. Absorption and scattering of light by small particles. New York: Wiley, 1983. p. 45–53.
[19] Pruppacher HP, Klett JD. Microphysics of clouds and precipitation. Netherland: Reidel, Dordrecht, 1980. 714pp.
[20] Arnott WP, Dong YY, Hallett J. Extinction efficiency in the infrared (2–18 μm) of laboratory ice clouds: observations of scattering minima in the Christiansen bands of ice. Appl Opt 1995;34:541–51.
[21] Francis PN, Jones A, Sauders RW, Shine KP, Slingo A, Sun Z. An observational and theoretical study of the radiative properties of cirrus: some results from ICE'89. Q J R Metero Soc 1994;120:809–48.
[22] Wyser K, Yang P. Average ice crystal size and bulk short-wave single-scattering properties of cirrus clouds. Atmos Res 1998;49:315–35.